Acta Materialia 232 (2022) 117957

Contents lists available at ScienceDirect

Acta Materialia

journal homepage: www.elsevier.com/locate/actamat

Full length article

On the exceptional creep resistance in a die-cast Gd-containing Mg alloy with Al addition

Xixi Dong[a,*], Lingyun Feng[a], Shihao Wang[a], Gang Ji[b], Ahmed Addad[b], Hailin Yang[c], Eric A. Nyberg[d], Shouxun Ji[a,*]

[a] Brunel Centre for Advanced Solidification Technology (BCAST), Brunel University London, Uxbridge UB8 3PH, UK
[b] CNRS, INRAE, Centrale Lille, UMR 8207 - UMET - Unité Matériaux et Transformations, University of Lille, Lille F-59000, France
[c] State Key Laboratory of Powder Metallurgy, Central South University, Changsha 410083, China
[d] Kaiser Aluminum, Spokane Valley, WA 99216, USA

ARTICLE INFO

Article history:
Received 12 February 2022
Revised 7 April 2022
Accepted 15 April 2022
Available online 18 April 2022

Keywords:
Magnesium alloy
Creep
Short-range order
Cluster
Mechanism

ABSTRACT

Over the past few decades, aluminium (Al) has been considered to be beneficial for castability but detrimental for the creep resistance of magnesium (Mg) alloys. However, an excellent creep resistance has been achieved in a die-cast Mg3.5RE(La,Ce,Nd)1.5GdMnAl alloy, with a super low steady-state creep rate (SCR) of 1.35 × $10^{-10}s^{-1}$ at 300 °C/50 MPa. Compared with the counterpart Al-free Mg3.5RE(La,Ce,Nd)1.5GdMn alloy, the SCR decreased by 71%. The synergistic effect of Al, Gd and Mn induced a novel thermally stable (TS) AlMnGd ternary short-range order (SRO, 0–2 nm)/cluster (2–10 nm) in the Mg matrix. After creep at 300 °C/50 MPa for 400 h, the AlMnGd SRO was still observed, and the AlMnGd clusters were under 10 nm and coherent with the Mg matrix. High density AlMnGd SRO/clusters were observed for pinning dislocations, which was the main reason for the improvement in the creep resistance in contrast to the counterpart Al-free alloy. The TS $Mg_{12}RE$(La,Ce,Nd) network at grain boundaries (GBs) impeded dislocation mobility, which also played an important role for the creep resistance compared to the traditional die-cast Mg-Al-based alloys. Under the critical conditions of 300 °C and 50–80 MPa, the creep still satisfied the power law, and the dominant creep mechanisms were SRO/cluster drag dislocation gliding, associated with GB diffusion. This work provides clear evidence for the long-term existence of some SRO/clusters in Mg alloys under critically high temperatures and stresses. Moreover, the utilization of AlMnGd SRO/clusters can be a novel approach for designing heat-resistant Mg alloys.

1. Introduction

Magnesium (Mg) alloys are excellent candidate materials for lightweight structures in the automobile, aerospace, rail and other industries when compared to steel and aluminium (Al) alloys [1–3]. Over the past few decades, one of the beneficial applications of magnesium alloys is the manufacturing of powertrain components, operating at the elevated temperatures of 150–200 °C [4–6]. Recently, this advancement has focused on the die-castable components in small internal combustion engines (SICE), used in machinery such as powered tools, drones and unmanned aerial vehicles, with a working temperature capable of reaching 200–300 °C, and where the creep resistance is a major challenge [7,8].

In the past, for Mg alloys, Al was considered beneficial for castability, but it was found to be detrimental for creep resistance at elevated temperatures [6,9,10]. The most widely used die-cast Mg alloys are Mg-Al-based alloys, such as AZ91, AM50 and AM60 because these Al-rich alloys have good die castability [11]. Unfortunately, the AZ and AM series die-cast Mg alloys are not suitable for elevated temperature applications above 120 °C due to the formation of a thermally unstable $Mg_{17}Al_{12}$ phase that is unbeneficial to creep resistance [12,13]. Considerable efforts were made to improve the creep resistance of the Al-rich die-cast Mg alloys via the addition of Si, Sr, Ca, Sn and rare earth (RE) to suppress the formation of $Mg_{17}Al_{12}$ [6,14]. The representative alloys are Mg-3Al-Si (AS31, compositions in the text are in wt.% unless specified) [15], Mg-Al-Sr (AJ62, AJ52) [16], Mg-8Al-1Ca-Zn (MRI153A) [17], Mg-4Al-1.2Ce-0.6La-0.4Nd (AE42) [18], Mg-8Al-1Ca-Sr (MRI153M) [19], Mg-4Al-2.5Ce-1.2La-0.5Nd (AE44) [14], Mg-6.5Al-2Ca-1Sn-Sr (MRI230D) [20,21] and Mg-4.5Al-3.5Ca-Sr (AXJ530) [22]. However, the improved die-cast Mg-Al-based alloys can generally only work at the elevated temperatures of 150–175 °C due to a significant increase in the creep rate when the temperature surpasses 175 °C [6,9]. It is generally believed [14] that the formation of thermally

* Corresponding authors.
E-mail addresses: Xixi.Dong@brunel.ac.uk (X. Dong), Shouxun.Ji@brunel.ac.uk (S. Ji).

https://doi.org/10.1016/j.actamat.2022.117957

unstable or non-interconnected Al-rich compounds such as Al_4Sr, Al_2Ca and $Al_{11}RE_3$ at the grain boundaries (GBs) restrict the die-cast Mg-Al-based alloys from working at higher temperatures. For die-cast Mg-Al-based alloys, the creep was dominated by grain boundary sliding (GBS) at low temperatures and applied stresses, while the dominant creep mechanisms could shift to dislocation climbing and cross-slip with the increase of temperatures to 150–175 °C [9,23].

One effective approach to improve elevated creep resistance is to develop Al-free die-cast Mg-RE alloys. The benchmarks are the La, Ce and/or Nd rich Mg-2.5Nd-0.3Zn-0.3Mn (MEZ) [24] and Mg-1.7La-1.0Ce-1.0Nd-0.45 Zn (AM-HP2+) alloys [10,14]. The RE content in die-cast Mg–RE alloys was usually lower than 4 wt.% as a high RE resulted in brittleness [6,10,25]. This restricted the die-cast Mg-RE alloys from working at higher temperatures, that is above 200 °C. It was thought [10] that the formation of thermally stable and interconnected $Mg_{12}RE$ compounds at the GBs benefited the creep resistance in Al-free die-cast Mg–RE alloys, and the addition of Al has been well reported for a deteriorating creep resistance in die-cast Mg-RE(La,Ce,Nd) alloys [10,26]. Further investigations disclosed that solute atoms and dynamic precipitation in the Mg matrix played important roles for creep resistance [27,28]. However, there is still intense debate about the effects of the solute atoms and precipitation on creep resistance [6]. The Mg-0.45La-1.2Y alloy was found to have a higher creep resistance in a solid solution state than in a solid solution and peak-aged condition, even though precipitates only existed in the Mg matrix of the aged alloy before creep [29]. The development of a short-range order (SRO) and cluster of solute atoms in the Mg matrix that could hinder dislocation movement was viewed as the dominant creep mechanism in this alloy system [30], but the SRO and cluster of solute atoms were considered as unstable and disappeared after ageing and/or creep in certain experiments [31,32]. In addition, nanoprecipitates rich in RE elements such as Y, Sm, Gd, Tb, Dy, Ho, Tm, Yb or Lu were observed in Al-*Sc* alloys, which could have positive effect on creep resistance [33–35].

Generally, the creep resistance of Mg alloys can be enhanced by the formation of thermally stable and interconnected compounds at the GBs [26,36], the solid solution of solute atoms [27,30,37] and/or the thermally stable precipitates [13,38,39] in the Mg matrix. However, the existing die-cast Mg alloys for elevated temperature applications go to two extremes of Al-rich and Al-free alloys. The Al-rich Mg alloys have a good castability. However, most of the atoms that are efficient at creep resistance are consumed by the Al to form thermally unstable and non-interconnected Al-rich phases at the GBs, rather than solid solution into the Mg matrix for solution or precipitation strengthening, which results in a poor creep resistance of Mg-Al-based alloys above 175 °C [6,13]. The Al-free die-cast Mg alloys, especially the Mg-RE(La,Ce,Nd) alloys, have a good creep resistance up to 200 °C that is associated with the thermally stable $Mg_{12}RE$(La,Ce,Nd) phase at the GBs [24,26]. Nonetheless, castability is a concern, and the resultant limited addition of RE restricts the strength of the alloys. Moreover, the Al-free and RE(Zn)-based precipitates formed in the Mg matrix of these alloys might not be as stable as some of the Al-containing precipitates [39,40]. For a long time, Al was viewed as unbeneficial for the creep resistance of Mg alloys; it is also hard to imagine a die-cast Mg alloy with a super creep resistance, especially at the higher temperatures of 200–300 °C, via the addition of Al in a die-cast Gd-containing Mg alloy.

In this work, an exceptional creep resistance has been achieved in our newly developed die-cast Gd-containing Mg3.5RE(La,Ce,Nd)1.5GdMnAl alloy [25,41], at the critically high temperature of 300 °C, via the addition of Al. The characterisation and mechanisms of the improvements in creep resistance in the Mg3.5RE(La,Ce,Nd)1.5GdMnAl alloy were closely studied at an atomic level to provide a new approach for designing heat-resistant Mg alloys.

2. Experimental

2.1. Material preparation

Cylindrical creep samples designed with ISO 204:2018 were prepared by high pressure die casting (HPDC) on a 4500 kN cold chamber machine; the gauge diameter and length of the creep samples were 6.35 mm and 20 mm, respectively. The newly developed die-cast Mg1.6La0.9Ce1.0Nd1.5Gd0.3Zn0.3Mn0.5Al (Mg3.5RE1.5GdMnAl) alloy was melted in a steel liner and held at 720 °C, under the mixed protection gas of N_2 (6 L/min) and SF_6 (0.025 L/min). The die and pour temperatures were controlled at 225 °C and 715 °C during HPDC. For comparison, the counterpart Al-free Mg1.6La0.9Ce1.0Nd1.5Gd0.3Zn0.3Mn (Mg3.5RE1.5GdMn) alloy and representative Mg-Al-based commercial die-cast alloys (MRI153M, AJ62, MRI230D and AE44) for elevated temperature applications were also melted and cast to make identical creep samples using the same HPDC.

2.2. Creep and tensile tests

Tensile creep tests were conducted on a lever-type Instron machine following ISO 204:2018. Several creep temperatures (200–300 °C) and stress levels (40–80 MPa) were applied for the creep tests. The temperature of the creep samples was controlled by thermocouples with an accuracy of ± 1 °C, and the loaded stresses were lower than the yield strength (YS) under different test temperatures. One extensometer was attached to the gauge section of the samples to measure the strains during a creep test. Three creep tests were performed for each condition. The tensile tests were performed using an Instron 5500 Testing System following ASTM E8 and E21 standards, and the initial ramp rates for room temperature (RT) and high temperature tensile tests were 1 mm/min and 0.0002/s, respectively.

2.3. Microstructure characterisation

Scanning electron microscopy (SEM) samples were prepared by mechanical grinding and polishing, and ethanol was applied during the grinding and polishing process to avoid surface corrosion. Backscattered SEM (BSD-SEM) observation was performed at 20 kV on a Zeiss SUPRA 35VP microscope. Electron backscatter diffraction (EBSD) samples were prepared by electrolytic polishing using picric acid solution (a mixture of 12.6 g picric acid, 30 ml acetic acid, 30 ml water and 420 ml ethanol) after mechanical polishing. The electrolyte temperature was −30 °C after liquid nitrogen treatment, and the polishing time was 80–100 s with 20 V voltage. Transmission electron microscopy (TEM) samples were prepared by mechanical polishing followed by final ion thinning. TEM analysis including nano-diffraction, bright-field (BF) imaging and high-resolution TEM (HRTEM) imaging were conducted using a FEI Tecnai G2 microscope. An in-depth TEM analysis was carried out on a Thermofisher Titan Themis 60–300 microscope operated at 300 kV. It was equipped with a highly efficient (4 quadrant) energy dispersive X-ray (EDX) system and a probe aberration corrector for atomic and nano-scale characterisation in the scanning TEM (STEM) mode. The collection angle of the high-angle annular dark field (HAADF) detector ranged from 80 to 150 mrad. The probe size was set to 0.1 nm with a convergent semi-angle of 22.5 mrad. Energy dispersive spectrometer (EDS) mapping was also applied under STEM. A 3D visualisation program for structural models, VESTA [42], was used to construct interfacial atomic structures.

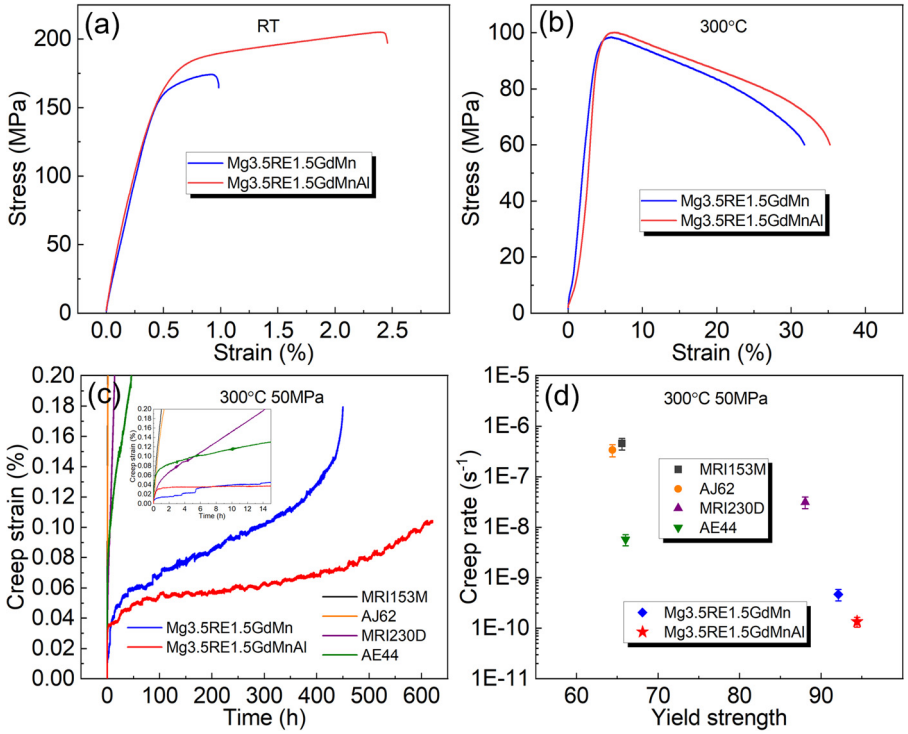

Fig. 1. Tensile and creep properties of the die-cast Mg3.5RE1.5GdMnAl alloy under as-cast condition. Representative tensile curves of the Mg3.5RE1.5GdMnAl alloy at (a) room temperature, (b) 300 °C and the comparison with the counterpart Al-free Mg3.5RE1.5GdMn alloy; (c) representative tensile creep curve and (d) steady-state creep rate of the Mg3.5RE1.5GdMnAl alloy tested at 300 °C with a 50 MPa stress, compared with the counterpart Al-free Mg3.5RE1.5GdMn alloy and the traditional representative Mg-Al-based commercial die-cast MRI153M, AJ62, MRI230D and AE44 alloys for elevated temperature applications.

3. Results

3.1. Tensile and creep properties

The representative tensile curves of the die-cast Mg3.5RE1.5GdMnAl alloy and the counterpart Al-free Mg3.5RE1.5GdMn alloy at RT and 300 °C are provided in Fig. 1a and b. The yield strength and ductility of the Mg3.5RE1.5GdMnAl alloy and the counterpart Mg3.5RE1.5GdMn alloy at RT were 165.3 ± 4.2 MPa and 2.45 ± 0.21%, 163.3 ± 3.8 MPa and 0.93 ± 0.24%, respectively. The addition of 0.5 wt.% Al led to a considerable improvement of 163% in RT ductility, which can reduce the susceptibility of the Mg3.5RE1.5GdMnAl alloy to cracking on ejection from the die. In addition, it is well accepted [4,5] in this industry that 2% is the required ductility for die-cast alloys. The yield strength and ductility of the Mg3.5RE1.5GdMnAl alloy and the counterpart Mg3.5RE1.5GdMn alloy at 300 °C were 94.4 ± 2.5 MPa and 32.5 ± 5.2%, 92.1 ± 2.3 MPa and 28.7 ± 5.0%, respectively.

Fig. 1c and d show the tensile creep properties of the die-cast Mg3.5RE1.5GdMnAl alloy, the comparison with the counterpart Al-free Mg3.5RE1.5GdMn alloy and the traditional representative Mg-Al-based commercial die-cast MRI153M, AJ62, MRI230D and AE44 alloys for elevated temperature applications. As illustrated in Fig. 1c, under the creep temperature of 300 °C and the stress of 50 MPa, the Mg3.5RE1.5GdMnAl alloy went into the tertiary state after creep for 460 h (h) and did not reach the rupture point after 620 h; the counterpart Mg3.5RE1.5GdMn alloy went into the tertiary state after creep for 350 h and ruptured after 450 h, whereas the secondary steady-state creep strain of the Mg3.5RE1.5GdMnAl alloy was much lower than the counterpart Mg3.5RE1.5GdMn alloy and the four commercial alloys. As shown in Fig. 1d, the steady-state creep rate (SCR, s^{-1}) of the MRI153M, AJ62, MRI230D, AE44, Mg3.5RE1.5GdMn and Mg3.5RE1.5GdMnAl alloys at 300 °C/50 MPa were $(4.58 \pm 1.19) \times 10^{-7}$, $(3.39 \pm 0.88) \times 10^{-7}$, $(3.15 \pm 0.82) \times 10^{-8}$, $(5.69 \pm 1.41) \times 10^{-9}$, $(4.68 \pm 1.23) \times 10^{-10}$ and $(1.35 \pm 0.28) \times 10^{-10}$, respectively. The Mg3.5RE1.5GdMnAl alloy showed a 71% reduction in the SCR compared with the counterpart Mg3.5RE1.5GdMn alloy; it further showed a much-improved creep resistance in contrast to the four typical Mg-Al-based commercial die-cast alloys. In addition, the SCR of the Mg3.5RE1.5GdMnAl alloy was lower than the heat-treated gravity cast Mg alloys (QE22, EQ21, AM-SC1, WE43, WE54, Mg15Gd, Mg8Gd4Y, Mg15Gd2Y, Mg10Gd3Y and Mg12Y5Gd) for applications at 200–300 °C [43–52]. Therefore, the die-cast Mg3.5RE1.5GdMnAl alloy has a super creep resistance that could increase the working temperatures of the die-cast Mg alloys from 120 to 200 °C [6,14] to 200–300 °C.

3.2. n/Q values determination of creep

In the secondary steady-state of creep, a near-constant creep rate is normally achieved, that is the steady-state creep rate (SCR, $\dot{\varepsilon}$), which can be described by the power law equation as follows [9]:

$$\dot{\varepsilon} = A\sigma^{n} \exp\left(-\frac{Q}{RT}\right) \quad (1)$$

Where A is a constant, σ is the applied stress, n is the stress exponent and Q is the activation energy for creep, T is the absolute temperature and R is the gas constant. For n, it is generally accepted that the dominant steady-state creep mechanisms of Mg alloys are diffusional creep ($n = 1$), GBS ($n = 2$) and dislocation creep ($n = 3$–7); $n = 3$ indicates solute atom or precipitate drag dislocation gliding, while $n = 4$–7 demonstrates dislocation gliding and climbing [6]. For Q, the main steady-state creep mechanisms of Mg alloys are GBS ($Q = 40$–60 kJ/mol), GB diffusion (GBD) ($Q = 60$–80 kJ/mol), pipe diffusion through dislocations ($Q = 92$ kJ/mol),

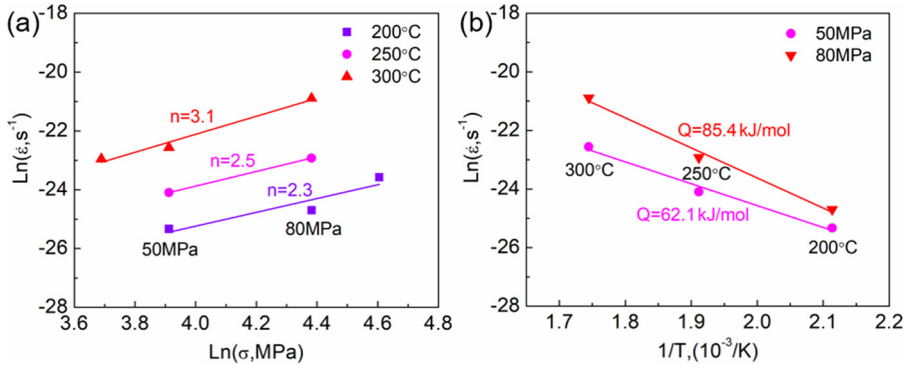

Fig. 2. (a) Steady-state creep rate plotted against applied stress and (b) temperature dependence of the steady-state creep rate for the determination of the n and Q values in the power-law equation for the die-cast Mg3.5RE1.5GdMnAl alloy during creep.

self-diffusion of Mg (Q = 135 kJ/mol) and cross-slip (Q = 229–325 kJ/mol) [9]. At higher creep temperatures and applied stresses, the breakdown of the power law can happen, which can be determined by Eqs. (2) and (3) [6]:

$$\dot{\varepsilon}/D > 10^{13}\mathrm{m}^{-2} \tag{2}$$

$$D = 10^{-4}\exp\left(-\frac{Q_L}{RT}\right)\left(\mathrm{m}^2\mathrm{s}^{-1}\right) \tag{3}$$

Where Q_L is the activation energy of the self-diffusion of Mg (135 kJ/mol).

Fig. 2a shows the variation of $\mathrm{Ln}\dot{\varepsilon}$ versus $\mathrm{Ln}\sigma$, and n was determined as 2.3, 2.5 and 3.1 at 200 °C, 250 °C and 300 °C, respectively. Fig. 2b presents the evolution of $\mathrm{Ln}\dot{\varepsilon}$ versus $1/T$ under different creep stresses. At the creep temperature range of 200–300 °C, Q are 62.1 kJ/mol and 85.4 kJ/mol at 50 MPa and 80 MPa, respectively. At 200–250 °C and 50–80 MPa, n is 2.3–2.5, and Q (62.1–85.4 kJ/mol) is close to the activation energy of GBD [9], indicating that the dominant steady-state creep mechanisms are GBS and GBD. At 300 °C and 50–80 MPa, n increases to 3.1 while Q maintains at 62.1–85.4 kJ/mol, demonstrating that the dominant steady-state creep mechanisms are drag dislocation gliding and GBD, in which the dislocation gliding can be mainly dragged by the AlMnGd SRO/clusters (see Fig. 11b). At the critical creep conditions of 300 °C/50–80 MPa, $\dot{\varepsilon}/D$ (0.32–1.71 × 10^7 m^{-2}) is less than 10^{13} m^{-2}, indicating that creep still satisfies the power-law.

3.3. Microstructure evolution by creep

3.3.1. Overall morphology

Fig. 3a and b present the as-cast microstructure of the die-cast Mg3.5RE1.5GdMnAl alloy before creep. The microstructure comprised the primary α_1_Mg matrix phase with a grain size of ~10–30 μm, the secondary α_2_Mg matrix phase with a grain size of ~2–10 μm and the network of intermetallic phases at the GBs. Previous studies [14,25] have confirmed that the fine α_2_Mg was formed in die cavity with a higher cooling rate than the α_1_Mg which was formed in a shot sleeve. The main body of the network at the GBs was the $Mg_{12}RE$ phase, while the blocky phase at the GBs was Al_2RE_3 (see Fig. 3b); moreover, the two intermetallic phases were determined by the composition and diffraction analysis in Sections 3.3.2 and 3.3.3. Fig. 3c and d present the microstructure of the Mg3.5RE1.5GdMnAl alloy after creep at 300 °C/50 MPa for 400 h. The $Mg_{12}RE$ and Al_2RE_3 phases at the GBs showed no visible change in morphology in comparison to the phases before creep. A novel AlMnGd ternary SRO/cluster was observed in the Mg matrix of the alloy both before and after creep, whereas the plate-like Al_2Gd precipitate appeared in the Mg matrix of the alloy after creep (see Figs. 3d, 6h, 8 and 11b). The AlMnGd SRO/cluster and Al_2Gd precipitate are further analysed in Sections 3.3.4 and 3.4. A reported feature of denuded zones (DZ) of precipitates near the GBs of a Mg-Gd alloy [53] was also observed (see Fig. 3d).

3.3.2. Mapping of the intermetallic phases at the GBs

Fig. 4a–i show the STEM/EDS mapping of elemental distributions at the GBs of the as-cast Mg3.5RE1.5GdMnAl before creep. The $Mg_{12}RE$ phase was enriched by La, Ce, Nd, Zn and Mn, while the Al_2RE_3 phase was enriched by Gd, Nd, La, Ce, Al, Mn and Zn. At the GBs, Al and Gd were preferred to precipitate in the Al_2RE_3 phase. The enrichment of Nd, Mn and Zn in the Al_2RE_3 phase was higher than that in the $Mg_{12}RE$ phase, while the enrichment of the La and Ce in Al_2RE_3 and $Mg_{12}RE$ phases were similar. Fig. 4j–r display the elemental distributions at the GBs of the die-cast Mg3.5RE1.5GdMnAl alloy after creep at 300 °C/50 MPa for 400 h, which are similar to the distributions before creep. The measured compositions of the $Mg_{12}RE$ and Al_2RE_3 intermetallic phases before and after creep are listed in Table 1. The atomic ratio of Mg:RE in $Mg_{12}RE$ was approximately 12:1, and the atomic ratio of Al:RE in Al_2RE_3 was approximately 2:3. There was nearly no change in composition in the two intermetallic phases after creep.

3.3.3. Diffraction of the intermetallic phases at the GBs

Fig. 5a–f present the diffraction patterns of the $Mg_{12}RE$ and Al_2RE_3 phases at the GBs of the die-cast Mg3.5RE1.5GdMnAl alloy before and after creep at 300 °C/50 MPa for 400 h, respectively. $Mg_{12}RE$ has been well determined in Mg-RE-based alloys [10,26], so one diffraction pattern was given here for $Mg_{12}RE$ (see Fig. 5a, d), which fits the diffraction pattern of $Mg_{12}Nd$ (Tetragonal, $a = b$ = 10.31 Å, c = 5.93 Å, Space group: I4/mmm [54]). Additionally, the {101} twins can be observed in the $Mg_{12}RE$ phase. The existence of the domains of the {101} twins in the $Mg_{12}RE$ phase has been well reported [55]. Two diffraction patterns were provided for Al_2RE_3 (see Fig. 5b, c, e and f), which agree with the diffraction pattern of Al_2Gd_3 (Tetragonal, $a = b$ = 8.344 Å, c = 7.656 Å, Space group: P42 nm [56]). The composition and diffraction analysis demonstrated that the phases at the GBs were $Mg_{12}RE$ and Al_2RE_3; moreover, there were no phase transformations at the GBs after creep, indicating that $Mg_{12}RE$ and Al_2RE_3 were stable and did not degrade at the high creep temperature of 300 °C.

3.3.4. Microstructure evolution in the Mg matrix

Fig. 6a–m show the microstructure in the Mg matrix of the Mg3.5RE1.5GdMnAl alloy before and after creep at 300 °C/50 MPa for 400 h, respectively. Isolated solute atoms and a novel ternary AlMnGd SRO/cluster were observed in the Mg matrix of the alloy before creep (Fig. 6a–g). After creep at 300 °C/50 MPa for 400 h,

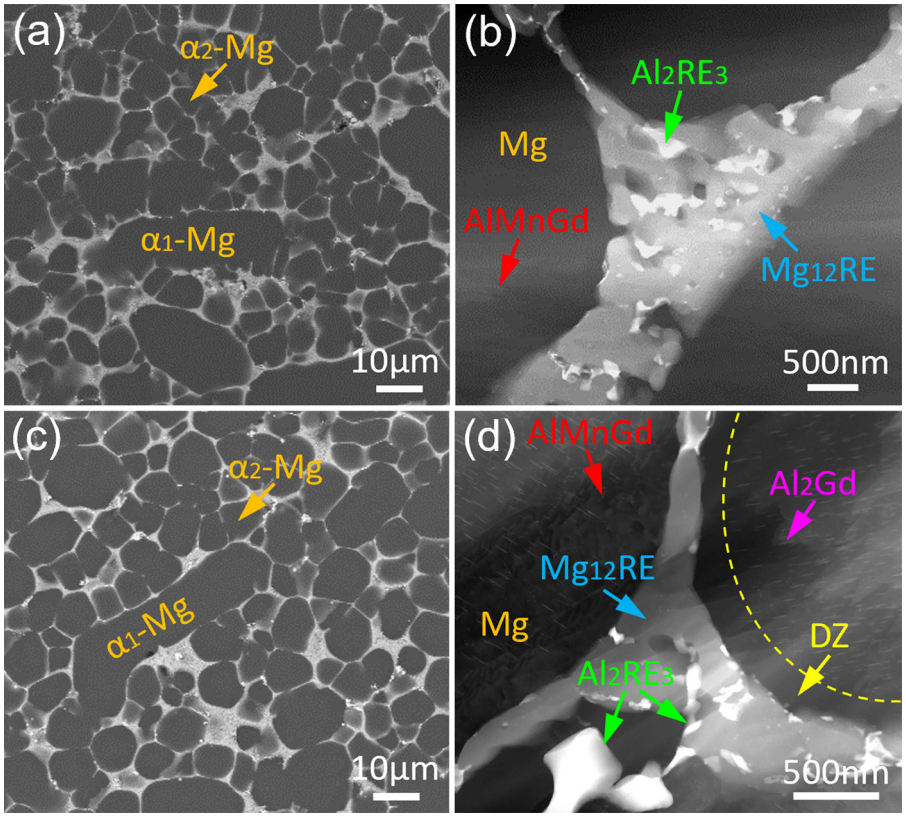

Fig. 3. Microstructure of the as-cast die-cast Mg3.5RE1.5GdMnAl alloy (a,b) before creep and (c,d) after creep at 300 °C/50 MPa for 400 h. (a,c) BSD-SEM morphology; (b,d) STEM images showing the intermetallic phases at the GBs and the changes in the Mg matrix of the crept microstructure.

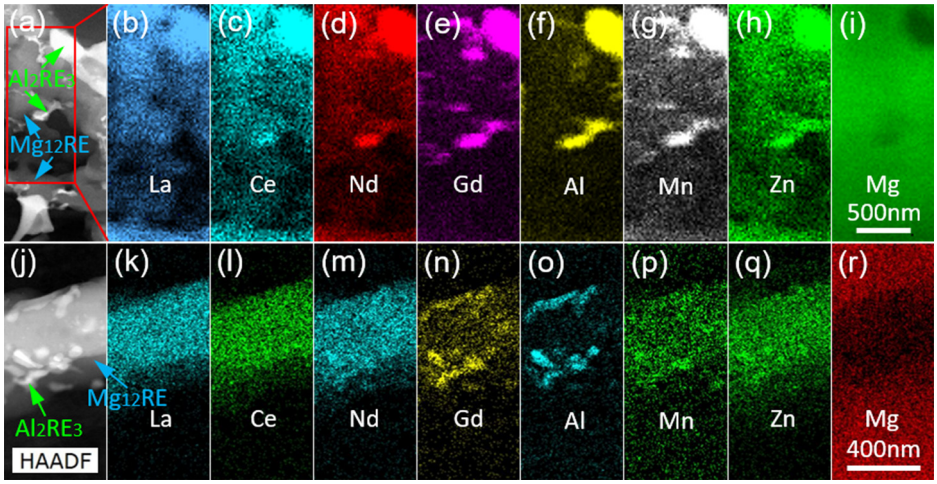

Fig. 4. STEM/EDS mapping of the elemental distributions at the GBs of the die-cast Mg3.5RE1.5GdMnAl alloy (a–i) before creep and (j–r) after creep at 300 °C/50 MPa for 400 h. (a,j) STEM images of the $Mg_{12}RE$ and Al_2RE_3 phases at the GBs; (b-i) maps of La, Ce, Nd, Gd, Al, Mn, Zn and Mg in the area marked by the box in (a); (k–r) maps of La, Ce, Nd, Gd, Al, Mn, Zn and Mg in (j).

Table 1
Measured compositions (in at.%) by STEM/EDS for the $Mg_{12}RE$ and Al_2RE_3 intermetallic phases at the GBs of the die-cast Mg3.5RE1.5GdMnAl alloy before and after creep at 300 °C/50 MPa for 400 h.

Intermetallic phases	La	Ce	Nd	Gd	Al	Mn	Zn	Mg
$Mg_{12}RE$ (Before creep)	2.3 ± 0.2	1.8 ± 0.2	2.1 ± 0.2	1.0 ± 0.1	0.9 ± 0.1	1.6 ± 0.2	2.4 ± 0.2	87.9 ± 0.4
$Mg_{12}RE$ (After creep)	2.5 ± 0.3	1.8 ± 0.2	1.9 ± 0.2	1.2 ± 0.1	0.8 ± 0.1	1.6 ± 0.2	2.5 ± 0.3	87.7 ± 0.5
Al_2RE_3 (Before creep)	2.7 ± 0.3	2.3 ± 0.2	7.9 ± 0.7	15.1 ± 1.1	18.9 ± 1.4	9.2 ± 0.9	8.3 ± 0.8	35.6 ± 1.5
Al_2RE_3 (After creep)	3.0 ± 0.3	2.2 ± 0.2	7.7 ± 0.7	15.4 ± 1.2	18.7 ± 1.3	9.1 ± 0.8	8.6 ± 0.9	35.3 ± 1.3

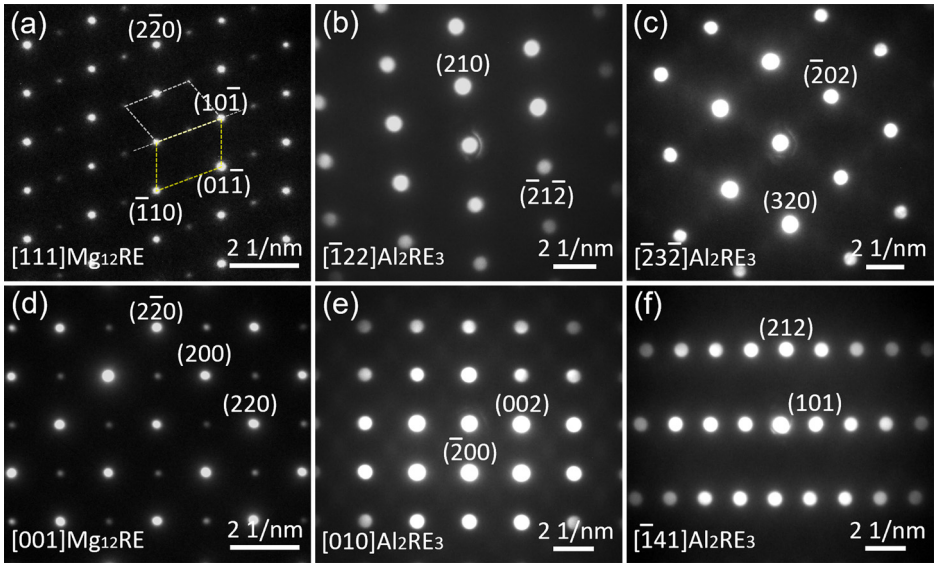

Fig. 5. Diffraction patterns of the intermetallic phases at the GBs of the die-cast Mg3.5RE1.5GdMnAl alloy (a–c) before creep and (d–f) after creep at 300 °C/50 MPa for 400 h. (a) The diffraction pattern of a $Mg_{12}RE$ twin observed along the [111] zone axis; (b, c) diffraction patterns of Al_2RE_3 observed along the [$\bar{1}$22] and [$\bar{2}$3$\bar{2}$] zone axes; (d) the diffraction pattern of a $Mg_{12}RE$ twin observed along the [001] zone axis; (e, f) diffraction patterns of Al_2RE_3 observed along the [010] and [$\bar{1}$41] zone axes.

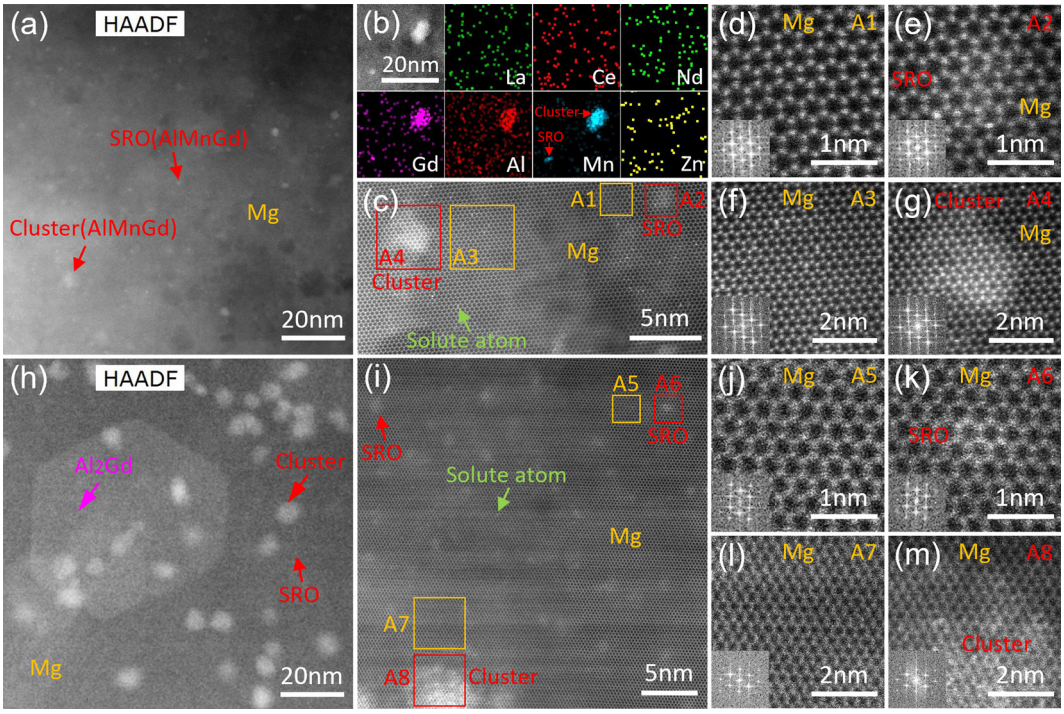

Fig. 6. STEM images showing the microstructure in the Mg matrix of the die-cast Mg3.5RE1.5GdMnAl alloy (a–g) before creep and (h–m) after creep at 300 °C/50 MPa for 400 h, under the projection direction of <0001>Mg. (a, c–g) The STEM-HAADF images and (b) STEM/EDS mapping of the solute atoms and AlMnGd SRO/clusters in the Mg matrix before creep; (h-m) the STEM-HAADF images showing the solute atoms, AlMnGd SRO/clusters and Al_2Gd precipitates in the Mg matrix after creep.

Al_2Gd precipitate was observed in the Mg matrix (Fig. 6h); isolated solute atoms and the AlMnGd SRO/clusters still existed in the Mg matrix (Fig. 6h–m); the quantity of isolated solute atoms decreased (Fig. 6i), while the size of some clusters increased (Fig. 6h). However, the size of the clusters was under 10 nm after creep at 300 °C/50 MPa for 400 h (Fig. 6h). In this work, the AlMnGd microstructure with the size of 0–2 nm and 2–10 nm was called the SRO and cluster, respectively. In addition, the size of Al_2Gd precipitate was ~27–75 nm (see Supplementary Fig. S1). Further, the Al_2Gd precipitate exhibited a hexagon-faceted morphology under the projection direction of <0001>Mg. Fig. 6d–g show the enlarged view of the areas marked by A1, A2, A3 and A4 in Fig. 6c, and j–m show the enlarged view of the areas marked by A5, A6, A7 and A8 in Fig. 6i. The AlMnGd SRO/clusters occupied the positions of the Mg atoms, both before (Fig. 6d–g) and after creep (Fig. 6j–m). The inserts in Fig. 6d–g and j–m show the corresponding fast Fourier transform (FFT) patterns in the areas, and the FFT patterns of the AlMnGd SRO/clusters were the same as their adjacent areas of Mg matrix, both before and after creep, which indicated that the AlMnGd SRO/clusters were coherent with the Mg matrix. SRO and clusters were also reported in some Mg alloys [29,30,57]. Therefore, the microstructure evolution mainly occurred in the Mg

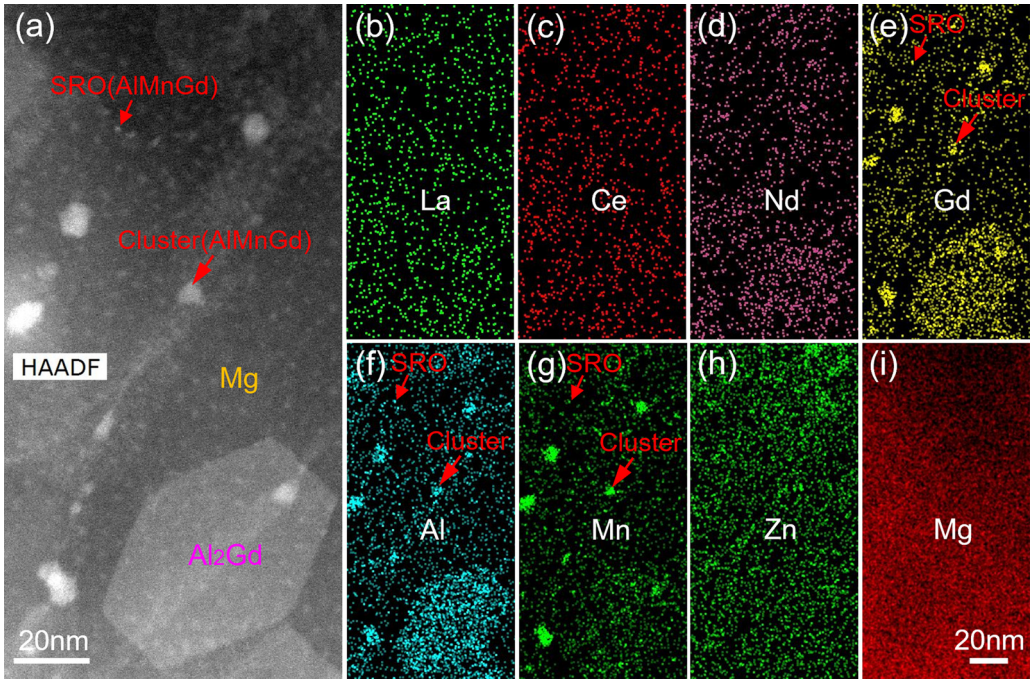

Fig. 7. STEM/EDS mapping of the elemental distributions in the Mg matrix of the die-cast Mg3.5RE1.5GdMnAl alloy after creep at 300 °C/50 MPa for 400 h. (a) The STEM-HAADF image of the Al_2Gd precipitate and AlMnGd SRO/cluster in the Mg matrix under the projection direction of $<10\bar{1}1>$Mg; (b–i) STEM/EDS maps of the elements: (b) La, (c) Ce, (d) Nd, (e) Gd, (f) Al, (g) Mn, (h) Zn and (i) Mg in (a).

Table 2
Measured compositions (in at.%) by STEM/EDS for the Al_2Gd precipitates and AlMnGd clusters in the Mg matrix of the die-cast Mg3.5RE1.5GdMnAl alloy after creep at 300 °C/50 MPa for 400 h.

Particle	La	Ce	Nd	Gd	Al	Mn	Zn	Mg
Al_2Gd	0.34 ± 0.03	0.66 ± 0.05	1.56 ± 0.14	2.47 ± 0.23	9.94 ± 0.86	1.37 ± 0.14	0.59 ± 0.07	83.07 ± 0.88
AlMnGd	0.17 ± 0.02	0.28 ± 0.03	0.31 ± 0.03	1.58 ± 0.14	9.22 ± 0.82	7.86 ± 0.72	0.42 ± 0.05	80.16 ± 0.84

matrix after creep. Details of the composition and atomic-resolution structure of the Al_2Gd precipitate and AlMnGd clusters after creep are discussed in Section 3.4.

3.4. Microstructure in the crept Mg matrix

3.4.1. Elemental distribution in the Mg matrix

Fig. 7 displays the STEM/EDS mapping of the elemental distributions in the Mg matrix of the die-cast Mg3.5RE1.5GdMnAl alloy after creep at 300 °C/50 MPa for 400 h. Fig. 7a shows the STEM-HAADF image of the Al_2Gd precipitate and AlMnGd SRO/cluster in the Mg matrix under a different projection direction of $<10\bar{1}1>$Mg, which was 46.8° from $<0001>$Mg. The observed morphology of the Al_2Gd precipitate accordingly changed a little from Fig. 6h. In addition, the AlMnGd cluster was still seen in granular morphology with a size less than 10 nm. Fig. 7b–i show the corresponding STEM/EDS maps of the elements La, Ce, Nd, Gd, Al, Mn, Zn and Mg in Fig. 7a, sequentially. The Al_2Gd precipitate was enriched in Al and Gd while the AlMnGd SRO/cluster was enriched in Al, Mn and Gd. The measured composition of the Al_2Gd precipitate by STEM/EDS is presented in Table 2. Note the compositions shown in Table 2 are relative values rather than absolute values as the effect of the Mg matrix could not be eliminated during the STEM/EDS measurement. Also, the compositions given by STEM/EDS were semi-quantitative, rather than 100% accurate since the measurement was inevitably affected by the channelling of electrons along atomic columns in zone axis conditions [58]. However, a repeatable atomic ratio of Al:RE(Gd,Nd,Ce,La) as ~2:1 could be clearly detected for a group of Al_2Gd precipitates by STEM/EDS (see Table 2); the Al_2Gd precipitate can be approximately written as $Al_2Gd_{0.5}Nd_{0.31}Ce_{0.13}La_{0.07}$. Further confirmation of the Al_2Gd precipitate was achieved by an atomic-resolution study, as discussed in Section 3.4.2. An obvious difference between the Al_2Gd precipitate and AlMnGd cluster was that the concentration of Mn in the AlMnGd cluster was much higher than in the Al_2Gd precipitate, as shown in Fig. 7g. Considering that the AlMnGd cluster was much smaller than the Al_2Gd precipitate in size, the semi-quantitative composition of the AlMnGd cluster was investigated by STEM/EDS under a higher resolution later.

3.4.2. Atomic structure of the Al_2Gd precipitate

Fig. 8 presents the typical atomic structure of the interface between the plate-like Al_2Gd precipitate and Mg matrix in the die-cast Mg3.5RE1.5GdMnAl alloy after creep at 300 °C/50 MPa for 400 h, which was observed under the projection direction of $[111]Al_2Gd//[0001]Mg$. The atomic-resolution STEM-HAADF images in Fig. 8a and b show that the Al_2Gd precipitate has a hexagon-faceted morphology, with $\{11\bar{2}\}Al_2RE//\{2\bar{1}\bar{1}0\}Mg$ or $<11\bar{2}>Al_2RE//<2\bar{1}\bar{1}0>Mg$. Fig. 8c shows the corresponding FFT pattern of the Al_2Gd/Mg interface illustrated in Fig. 8a. It can be seen that the FFT pattern of the Al_2Gd precipitate nearly coincided with that of the Mg matrix, indicating a very small misfit between the Al_2Gd precipitate and Mg matrix in the two-dimensional (2D) hexagon plane that is perpendicular to $[111]Al_2Gd$ or [0001]Mg. Fig. 8d presents the simulated atomic structure model of the Al_2Gd/Mg interface under the same projection direction of $[111]Al_2Gd//[0001]Mg$, based on the standard unit cells of Mg and Al_2Gd (face-centred cubic, a = 7.899 Å, Space group: Fd-3 m [59]), which agrees with the results shown in Fig. 8b. The theoretical in-plane ($\perp$[0001]Mg) misfit between

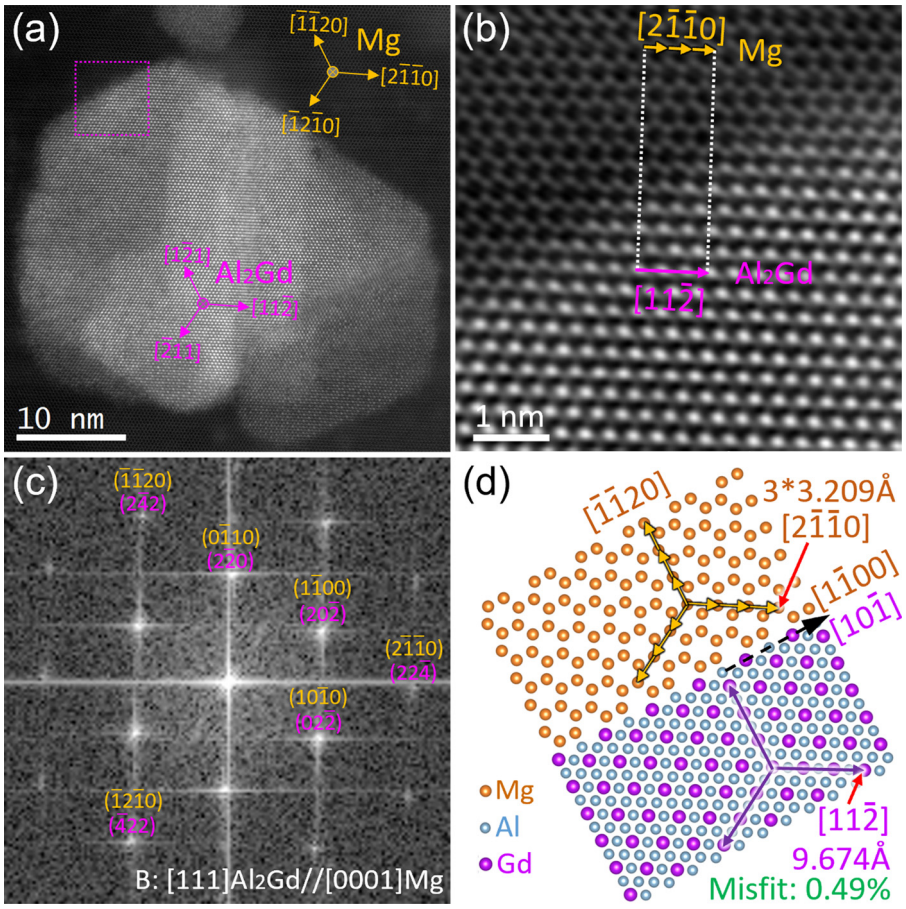

Fig. 8. (a) Atomic-resolution STEM-HAADF image showing the plate-like Al_2Gd precipitate in the Mg matrix of the die-cast Mg3.5RE1.5GdMnAl alloy after creep at 300 °C/50 MPa for 400 h, observed along the zone axis [111]Al_2Gd//[0001]Mg; (b) enlarged view of the Al_2Gd/Mg interface marked by a dotted box in (a); (c) FFT pattern of the Al_2Gd/Mg interface in (a); (d) simulated atomic structure model showing the Al_2Gd/Mg interface ({11$\bar{2}$}Al_2Gd//{2$\bar{1}\bar{1}$0}Mg, [10$\bar{1}$]Al_2Gd//[1$\bar{1}$00]Mg) in (a, b). All projection directions are [111]Al_2Gd//[0001]Mg.

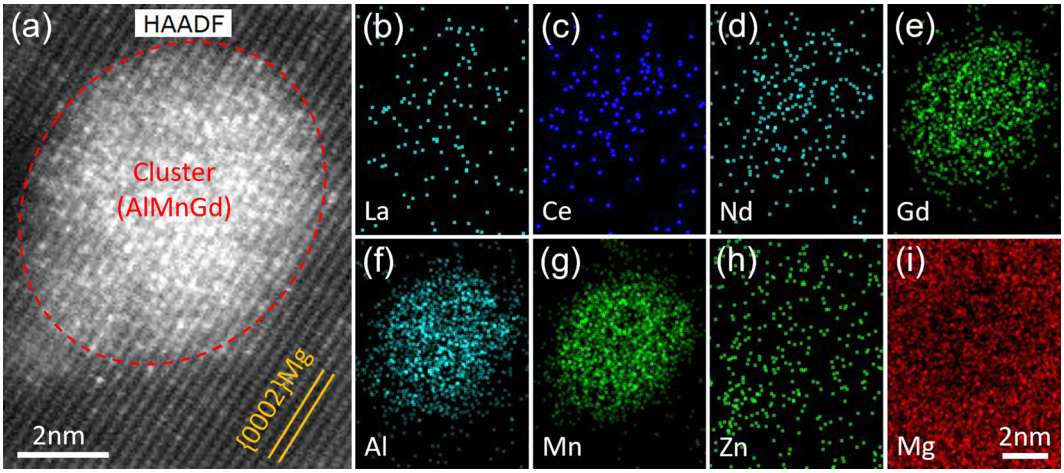

Fig. 9. STEM/EDS mapping of the AlMnGd cluster in the Mg matrix of the die-cast Mg3.5RE1.5GdMnAl alloy after creep at 300 °C/50 MPa for 400 h. (a) Atomic-resolution STEM-HAADF image showing the AlMnGd cluster in the Mg matrix, observed along the zone axis of [10$\bar{1}$0]Mg; (b-i) STEM/EDS maps of the elements: (b) La, (c) Ce, (d) Nd, (e) Gd, (f) Al, (g) Mn, (h) Zn and (i) Mg in (a).

the Al_2Gd precipitate and Mg matrix along the directions of <11$\bar{2}$>Al_2Gd//<2$\bar{1}\bar{1}$0>Mg is only 0.49%.

3.4.3. AlMnGd clusters in the Mg matrix

Fig. 9 displays a high-resolution STEM/EDS mapping of the AlMnGd cluster in the Mg matrix of the die-cast Mg3.5RE1.5GdMnAl alloy after creep at 300 °C/50 MPa for 400 h. The AlMnGd cluster was enriched by Al, Mn and Gd, and the concentrations of Al and Mn were higher than Gd in the cluster (see Fig. 9b–i). The measured composition of the AlMnGd cluster by STEM/EDS is listed in Table 2, i.e., 9.22at.%Al, 7.86at.%Mn, 1.58at.%Gd, 0.31at.%Nd, 0.28at.%Ce, 0.17at.%Ce and 0.42at.%Zn.

Fig. 10a–c present the atomic-resolution STEM-HAADF images of the AlMnGd clusters in the Mg matrix of the die-cast

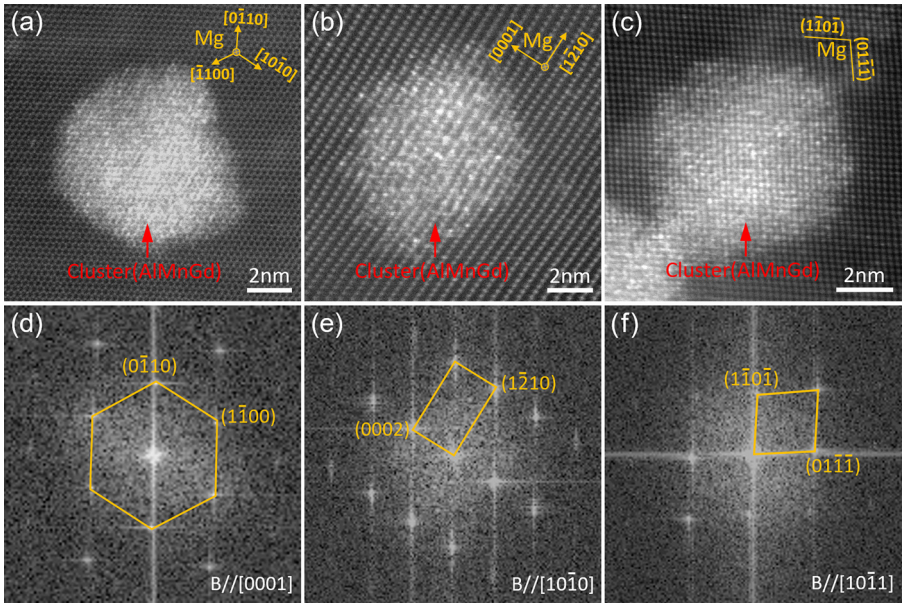

Fig. 10. Atomic-resolution STEM-HAADF imaging from three directions of the AlMnGd clusters in the Mg matrix of the die-cast Mg3.5RE1.5GdMnAl alloy after creep at 300 °C/50 MPa for 400 h. (a), (b) and (c) are atomic-resolution STEM-HAADF images of the AlMnGd clusters in the Mg matrix, observed along the zone axes of [0001]Mg, [10$\bar{1}$0]Mg and [10$\bar{1}$1]Mg, respectively; (d), (e) and (f) are FFT patterns corresponding to the AlMnGd cluster and Mg matrix in (a), (b) and (c), respectively.

Mg3.5RE1.5GdMnAl alloy after creep at 300 °C/50 MPa for 400 h, under three different projection directions of [0001]Mg, [10$\bar{1}$0]Mg and [10$\bar{1}$1]Mg, respectively. [10$\bar{1}$1]Mg and [10$\bar{1}$0]Mg were 46.8° and 90° from [0001]Mg, respectively. The AlMnGd clusters were granular under all the three projection directions, demonstrating that AlMnGd clusters are near spherical. In addition, the AlMnGd clusters were observed as being coherent with the Mg matrix (see Fig. 10a–c), which was also verified by the corresponding FFT patterns in Fig. 10d–f. Furthermore, the AlMnGd clusters were still far from forming a clear unit cell structure with corresponding diffraction patterns (see Fig. 10d–f) after creep at 300 °C/50 MPa for a duration of 400 h; they can also be considered clusters that have occupied the positions of the Mg atoms (see Fig. 10a–c).

4. Discussion

4.1. Stability of the precipitate and SRO/cluster in the Mg matrix

After creep at 300 °C/50 MPa for 400 h, Al_2Gd precipitates showed limited growth to ~27–75 nm (see Fig. 6h); the size of the AlMnGd SRO/clusters did not exceed 10 nm (see Figs. 6h and 7a), indicating the excellent coarsening resistance and thermal stability of these two, especially the AlMnGd SRO/clusters. Al_2RE had the maximum thermal stability among the Al-RE serials compounds, due to its lowest negative formation energy of −0.46 eV/atom [60,61]. It also has a melting point of ~1200 °C [2]. As discussed in Section 3.4.1, the Al_2Gd precipitates are enriched by Gd that has a strong combination with Al [30,61]. The Al-Mn dynamic precipitates can improve the creep resistance of the die-cast Mg-Al-based alloys, such as Mg-4Al-4RE-0.3Mn [39]. Further, the Al_8Mn_5 precipitate was identified in these alloys [40]. From the Al-Mn-RE ternary phase diagram, Al_8Mn_4RE is a possible constituent. It was reported [62] that the addition of Y resulted in the precipitation of Al_8Mn_4RE in a heat-treated AZ31–0.5Ca-0.25Y alloy, instead of Al_8Mn_5, demonstrating that Al_8Mn_4RE is more stable than Al_8Mn_5. The addition of Gd led to the formation of the AlMnGd clusters (see Fig. 9) with a semi-quantitative composition of $Al_{9.22}Mn_{7.86}RE_{2.34}(Gd_{1.58}Nd_{0.31}Ce_{0.28}La_{0.17})$ (see Table 2), which has been shown to be very close to the $Al_{10}Mn_7RE_2$ phase [63,64]. Note that the $Al_{10}Mn_7RE_2$ intermetallic phase was located at the GBs, rather than in the Mg matrix in these reports. The formation energy of the $Al_xMn_yRE_z$ phases can be determined as follows:

$$\Delta H = (E_{total} - xE_{Al} - yE_{Mn} - zE_{RE})/(x + y + z) \quad (4)$$

Where E_{total} is the total energy, E_{Al}, E_{Mn} and E_{RE} are the ground state energies per atom of Al, Mn and RE, and x, y and z are the numbers of the Al, Mn and RE atoms, respectively.

As can be seen in Eq. (4), the formation energies of the $Al_{10}Mn_7RE_2$ and Al_8Mn_4RE phases were calculated as −2.17 eV/atom and −1.90 eV/atom [65], respectively, indicating that $Al_{10}Mn_7RE_2$ can be more stable than Al_8Mn_4RE. Therefore, the thermal stability of these three Al-Mn(RE) precipitates is $Al_{10}Mn_7RE_2$ > Al_8Mn_4RE > Al_8Mn_5, and the approximate $Al_{10}Mn_7Gd_2$ clusters formed here are very stable among the possible series of Al-Mn-Gd precipitates. The approximate $Al_{10}Mn_7Gd_2$ clusters can be more stable than the Al_2Gd precipitates, as the formation energy of $Al_{10}Mn_7Gd_2$ (−2.17 eV/atom) is much lower than that of Al_2Gd (−0.46 eV/atom) [60,61,65]. As illustrated in Fig. 10, the approximate $Al_{10}Mn_7Gd_2$ clusters are still in the early stage of clustering without any clear unit cell structure or corresponding FFT pattern. The alloy has been crept under the critical conditions of 300 °C/50 MPa for a duration of 400 h, further demonstrating the high thermal stability of the AMnGd SRO/clusters.

4.2. Precipitates/GBs and dislocation interaction

Fig. 11 shows the interactions between dislocations and precipitates in the Mg matrix, and between the dislocations and intermetallic phases at the GBs during the steady-state creep of the die-cast Mg3.5RE1.5GdMnAl alloy at 300 °C/50 MPa. Following the Burgers vector analysis method and the invisibility criteria of dislocations in Mg alloys [23], the dislocations were viewed with $\boldsymbol{g}$ = [10$\bar{1}$1]Mg (see Fig. 11a,b), g = [0002]Mg (see Fig. 11c) and g = [10$\bar{1}$0]Mg (see Fig. 11d), under the projection direction of [1$\bar{2}$10]Mg. The dislocations are aligned on both basal and non-basal planes of the Mg matrix when observed with g = [10$\bar{1}$1]Mg (see Fig. 11a). However, some of the dislocations become invisible when viewed with g = [0002]Mg (see Fig. 11c), indicating the

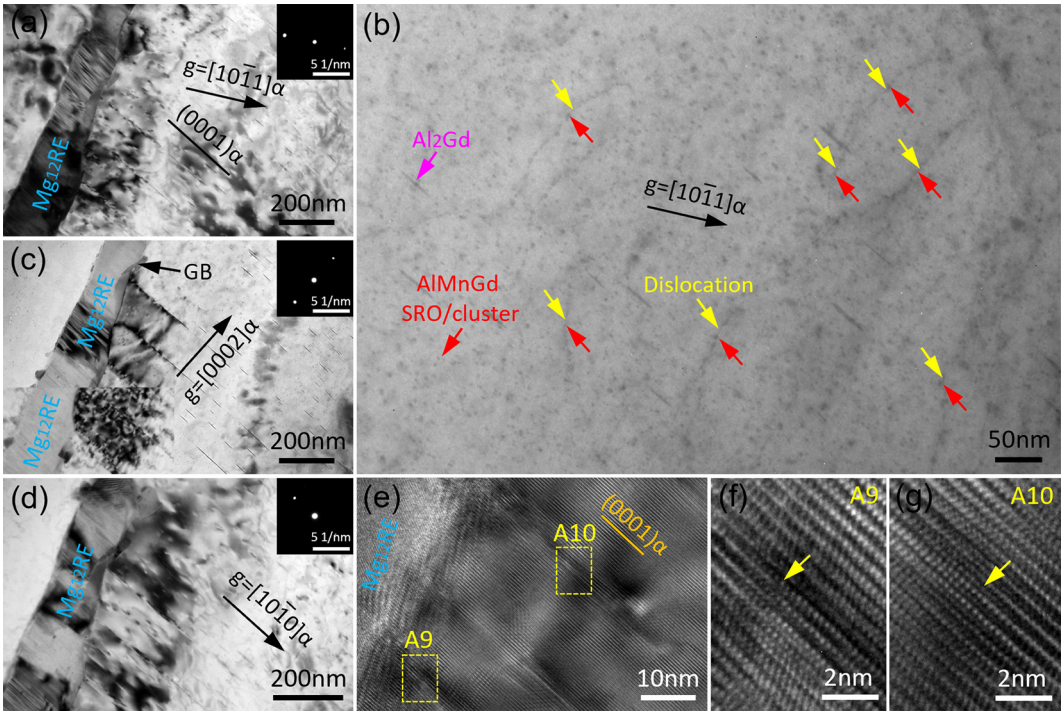

Fig. 11. (a–d) BF-TEM under two-beam conditions and (e–g) HRTEM images viewed along the [1$\bar{2}$10]Mg, showing the dislocations in the die-cast Mg3.5RE1.5GdMnAl alloy after creep at 300 °C/50 MPa for 400 h. (a, b) The dislocations viewed with g = [10$\bar{1}$1]Mg: (a) dislocations near the GBs; (b) dislocations far from the GBs, and dislocations pinning by high density AlMnGd SRO and clusters; (c) dislocations in a similar area to (a) and viewed with g = [0002]Mg, and the insert shows dislocation pile-up at the GBs; (d) dislocations in similar area to (a, c) and viewed with g = [10$\bar{1}$0]Mg; (e) HRTEM image showing the dislocations very near the GBs; (f) and (g) enlarged views of the dislocation areas marked by A9 and A10 in (e), respectively.

presence of ⟨a⟩ Burgers vector. The dislocations that are visible under g = [0002]Mg should have a ⟨c⟩ component. A further observation under g = [10$\bar{1}$0]Mg (see Fig. 11d) indicates that the dislocations having a ⟨c⟩ component are in the forms of both the ⟨c⟩ and ⟨a + c⟩ dislocations. Importantly, high density AlMnGd SRO/clusters were observed for pinning dislocations in the Mg matrix (see Fig. 11b). Al_2Gd precipitates can also contribute to dislocation pinning (see Fig. 11c); however, due to the lower number density and larger size, their contribution to the dislocation pinning may not be as significant as the AlMnGd SRO/clusters. Furthermore, a dislocation pile-up can be observed at the GBs (see Fig. 11c), which indicated that the Mg_{12}RE network at the GBs retarded any further motion of the dislocations. The HRTEM images in Fig. 11e–g show the impeding of the dislocations across the GBs by the Mg_{12}RE network.

4.3. Effects of the precipitates and SRO/clusters on creep

Dynamic precipitates were traditionally thought to contribute to the creep resistance of Mg alloys via dislocation pinning [28,38,39]. However, in some alloys such as Mg-0.45La-1.2Y (in at.%), SRO/clusters can play an important role for creep resistance [29]. There have been some intense debates about the effects of the dynamic precipitates and SRO/clusters on creep resistance [6]. Some researchers thought that SRO/clusters were thermally unstable and disappeared after ageing and/or creep [31,32]. Clearly, massive amounts of the AlMnGd SRO/clusters still existed in the Mg matrix of the die-cast Mg3.5RE1.5GdMnAl alloy, after creep at 300 °C/50 MPa for a duration of 400 h, which can be attributed to the high thermal stability of the AlMnGd SRO/clusters, as discussed in Section 4.1. SRO/clusters could also hinder dislocation movement and contribute to creep resistance [30,57]. Here, both the Al_2Gd precipitates (see Fig. 11c) and the AlMnGd SRO/clusters (see Fig. 11b) were observed for dislocation pinning in the Mg matrix, which can contribute to creep resistance. However, the number density (see Figs. 6h, 7a and 11b) and thermal stability (see Section 4.1) of the AlMnGd SRO/clusters were much higher than the Al_2Gd precipitates, so the AlMnGd SRO/clusters should play an important role for the creep resistance of the Mg3.5RE1.5GdMnAl alloy. The microstructure and composition analysis (see Supplementary Figs. S2 and S3) demonstrated that the addition of Al hardly changed the Mg_{12}RE network at the GBs, and it also did not change the content of other solute atoms in the Mg matrix, compared with the counterpart Al-free Mg3.5RE(La,Ce,Nd)1.5GdMn alloy. The combination of Al and Gd mainly resulted in two changes in the Mg3.5RE(La,Ce,Nd)1.5GdMnAl alloy: (1) forming the minority of the Al and Gd rich Al_2RE_3 phase at the GBs (see Figs. 3–5, Table 1 and Supplementary Fig. S2) that had a limited effect on creep; (2) forming a large number of thermally stable and creep-resistant AlMnGd SRO/clusters in the Mg matrix (see Figs. 6, 7, 9 and 11b, and Table 2). In addition, the STEM analysis results of the Mg matrix of the counterpart Al-free Mg3.5RE(La,Ce,Nd)1.5GdMn alloy before creep and after creep at 300 °C/50 MPa for 400 h are provided in Supplementary Fig. S4. SRO/clusters were hardly observed in the Mg matrix of the crept Mg3.5RE(La,Ce,Nd)1.5GdMn alloy, and REZn, ZnGd and MnGd precipitates dominated the creep of the alloy rather than SRO/clusters. Further, different from the AlMnGd SRO/clusters (<10 nm) in the Mg3.5RE(La,Ce,Nd)1.5GdMnAl alloy, the MnGd precipitates had a unit cell structure with corresponding FFT pattern, the size of the MnGd precipitates (~16–30 nm) was much larger, and the quantity of the MnGd precipitates was much lower, in the crept Mg3.5RE(La,Ce,Nd)1.5GdMn alloy (see Supplementary Fig. S4). These facts further verified the high thermal stability of the AlMnGd SRO/clusters and their dominant contribution to the 71% decrease of the steady-state creep rate in the Mg3.5RE(La,Ce,Nd)1.5GdMnAl alloy, in comparison with the Mg3.5RE(La,Ce,Nd)1.5GdMn alloy. Moreover, the

singular addition of Al into traditional Gd-free Mg-RE(La,Ce,Nd) alloys deteriorated creep resistance [10,26]. Therefore, it is not the singular effect of Al or Gd that provides the exceptional improvement of creep resistance; it is the synergistic effect of Al, Gd and Mn to form the novel thermally stable and creep-resistant ternary AlMnGd SRO/clusters in the Mg matrix that provides the exceptional improvement in the creep resistance in the Mg3.5RE(La,Ce,Nd)1.5GdMnAl alloy. This is in contrast to the counterpart Al-free Mg3.5RE(La,Ce,Nd)1.5GdMn alloy.

4.4. Effects of $Mg_{12}RE/Al_2RE_3$ at the GBs on creep

It was suggested that the formation of the $Mg_{12}RE$ phase at the GBs became possible in Mg-Al-RE alloys when the RE/Al weight ratio was above 1.4 [63]. In differentiation to the divorced or lamellar Al-containing compounds in the die-cast Mg-Al-based alloys, $Mg_{12}RE$ constitutes the major intermetallic phase at the GBs of the Al-free die-cast Mg-RE alloys [10,23]. More importantly, $Mg_{12}RE$ can form a network. With the increase of the RE/Al weight ratio, there is a transition from the Al-rich $Al_{11}RE_3$ to the Al-free $Mg_{12}RE$ at the GBs. In theory, the transition sequence is $Al_{11}RE_3 \rightarrow Al_2RE \rightarrow AlRE \rightarrow Al_2RE_3 \rightarrow AlRE_2 \rightarrow Mg_{12}RE$ [60]. As the die-cast Mg3.5RE1.5GdMnAl alloy has a RE/Al weight ratio of ~10:1, the $Mg_{12}RE$ network can form at the GBs (see Fig. 3). However, Al is tied up by RE, especially Gd, to form the divorced Al_2RE_3 compound at the GBs (see Fig. 4). $Mg_{12}RE$ was reported to be more stable than $Al_{11}RE_3$, which can degrade to Al_2RE via a releasing of Al [24,26]. The diffraction analysis after creep (see Fig. 5) also supported the stability of $Mg_{12}RE$. It was further reported [36] that the increase of the interconnectivity of the intermetallic phase at the GBs was important for the enhancement of creep resistance as it can shield more load from the matrix. Regarding Al_2RE_3, it is highly rich in RE, rather than Al, and it has the only theoretical possibility of decomposition into $AlRE_2$. However, this decomposition would not occur (see Fig. 5) even at 300 °C/50 MPa as the later lanthanides including Gd had a strong combination with Al [61]. Moreover, Al_2RE_3 has a melting point of more than 1000 °C [60]. Thus, in terms of the intermetallic phases at the GBs, the addition of Al here did not deteriorate the creep properties as Al was tied up by Gd to form the thermally stable Al_2RE_3 compound. Considering that the major phase at the GBs was the thermally stable network of $Mg_{12}RE$, $Mg_{12}RE$ should also play a significant part in the excellent creep resistance in the die-cast Mg3.5RE1.5GdMnAl alloy via impeding the movement of dislocations across the GBs (see Fig. 11c and e). This is in comparison to the traditional Mg-Al-based commercial die-cast alloys (see Fig. 1) for elevated temperature applications. However, for the counterpart Al-free Mg3.5RE1.5GdMn alloy, the addition of 0.5 wt.% Al should have a very limited effect on the improvement of creep resistance at the GBs since it hardly changed the major $Mg_{12}RE$ network at the GBs (see Supplementary Fig. S3 and Table S1). In addition, the grain size of the Mg3.5RE1.5GdMnAl alloy and the counterpart Al-free Mg3.5RE1.5GdMn alloy before creep were measured as 13.2 μm and 13.7 μm (see Supplementary Fig. S5), respectively, so the effect of grain size on the improvement of creep resistance was very limited. Furthermore, the grain size of the Mg3.5RE1.5GdMnAl and Mg3.5RE1.5GdMn alloys after creep at 300 °C/50 MPa for 400 h were measured as 13.6 μm and 14.2 μm (see Supplementary Fig. S5), respectively, and the grains did not grow much after creep.

Overall, the die-cast Mg3.5RE1.5GdMnAl alloy offers a super low steady-state creep rate of 1.35×10^{-10} s^{-1} under the critical condition of 300 °C/50 MPa, and it now enables the die-cast Mg alloys to work at the higher temperatures of 200–300 °C. Compared with the counterpart Al-free Mg3.5RE1.5GdMn alloy, the addition of 0.5 wt.% Al leads to a 71% reduction in the steady-state creep rate. It is the synergistic effect of Al, Gd and Mn in forming the novel thermally stable and creep-resistant ternary AlMnGd SRO/clusters in the Mg matrix that provides the exceptional improvement of creep resistance in the Mg3.5RE1.5GdMnAl alloy. This is in contrast to the counterpart Al-free Mg3.5RE1.5GdMn alloy, which alters the traditional understanding of the disadvantage of Al on the creep resistance of Mg alloys. The formation of a thermally stable network of the $Mg_{12}RE$(La,Ce,Nd) intermetallic phase at the GBs, which impedes dislocation mobility, also plays an important role in achieving the super creep resistance in the Mg3.5RE1.5GdMnAl alloy. This compares starkly with the traditional Mg-Al-based commercial die-cast alloys for elevated temperature applications. Therefore, this work can hopefully provide a novel approach for designing the high performance Mg alloys for higher elevated temperature applications, with the positive effects of Al on both castability and elevated mechanical properties.

5. Conclusions

(1) The die-cast Mg3.5RE1.5GdMnAl alloy offers a super-low steady-state creep rate of 1.35×10^{-10} s^{-1} under the critical condition of 300 °C/50 MPa, which is 71% lower than the counterpart Al-free Mg3.5RE1.5GdMn alloy, and much lower than the traditional Mg-Al-based commercial die-cast alloys for elevated temperature applications; this enables die-cast Mg alloys to work at the higher temperatures of 200–300 °C.

(2) The addition of Al induces the formation of a novel thermally stable ternary AlMnGd short-range order/cluster in the Mg matrix of the Gd-containing Mg3.5RE1.5GdMnAl alloy. The AlMnGd short-range order/clusters still exist after creep at 300 °C/50 MPa for 400 h. Moreover, high density AlMnGd short-range order/clusters can be observed for dislocation pinning during creep. It is the synergistic effect of Al, Gd and Mn to form the thermally stable and creep-resistant AlMnGd short-range order/clusters that provides the exceptional improvement of creep resistance in the Mg3.5RE1.5GdMnAl alloy in comparison to the counterpart Al-free Mg3.5RE1.5GdMn alloy; this alters the traditional understanding of the disadvantage of Al on the creep resistance of Mg alloys.

(3) A thermally stable network of the $Mg_{12}RE$(La,Ce,Nd) phase forms at the grain boundaries of the Mg3.5RE1.5GdMnAl alloy; it also impedes the further motion of dislocations across the grain boundaries, which plays a significant role in achieving the super creep resistance in the Mg3.5RE1.5GdMnAl alloy, in contrast to the traditional Mg-Al-based commercial die-cast alloys for elevated temperature applications. In addition, at the grain boundaries, Al is mainly tied up by Gd to form a minority of thermally stable RE-rich Al_2RE_3 compounds that do not degrade at the high creep temperature of 300 °C.

(4) The obtained n and Q values in the power law demonstrate that the dominant steady-state creep mechanisms of the die-cast Mg3.5RE1.5GdMnAl alloy under different creep temperatures and applied stresses are: a) grain boundary sliding and grain boundary diffusion at 200–250 °C/50–80 MPa (n = 2.3–2.5, Q = 62.1–85.4 kJ/mol); and b) short-range order/clusters drag dislocation gliding associated with grain boundary diffusion at 300 °C/50–80 MPa (n = 3.1, Q = 62.1–85.4 kJ/mol). Under the critical creep conditions of 300 °C/50–80 MPa, $\dot{\varepsilon}/D$ is $0.32–1.71 \times 10^7$ m^{-2}, and the creep of the die-cast Mg3.5RE1.5GdMnAl alloy still satisfies the power law.

Declaration of Competing Interest

The authors declare that they have no known competing financial interests or personal relationships that could have appeared to influence the work reported in this paper.

Acknowledgements

This work has been supported by Innovate UK (Project Ref.: 10004694) and Husqvarna Group. Dr. Changming Fang from Brunel University London is also greatly appreciated for the helpful discussions on phase stability. The TEM facility in Lille, France, supported by the Conseil Regional du Nord-Pas de Calais and the European Regional Development Fund (ERDF), is also acknowledged for conducting the atomic-resolution STEM-HAADF characterisation.

Supplementary materials

Supplementary material associated with this article can be found, in the online version, at doi:10.1016/j.actamat.2022.117957.

References

[1] K.U. Kainer, in: Magnesium Alloys and Technology, Wiley-VCH, Weinheim, 2003, pp. 2–28.
[2] M.O. Pekguleryuz, K. Kainer, A. Kaya, in: Fundamentals of Magnesium Alloy Metallurgy, Woodhead Publishing, Cambridge, 2013, pp. 1–168.
[3] I. Polmear, D. StJohn, J.F. Nie, M. Qian, in: Light Alloys: Metallurgy of the Light Metals, Butterworth-Heinemann, Oxford, 2017, pp. 3–38.
[4] A.A. Luo, Magnesium casting technology for structural applications, J. Magnes. Alloy. 1 (2013) 2–22.
[5] M. Easton, A. Beer, M. Barnett, C. Davies, G. Dunlop, Y. Durandet, S. Blacket, T. Hilditch, P. Beggs, Magnesium alloy applications in automotive structures, JOM 60 (2008) 57–62.
[6] N. Mo, Q.Y. Tan, M. Bermingham, Y.D. Huang, H. Dieringa, N. Hort, M.X. Zhang, Current development of creep-resistant magnesium cast alloys: a review, Mater. Des. 155 (2018) 422–442.
[7] N. Hort, H. Dieringa, K.U. Kainer, Magnesium pistons in engines: fiction or fact? Magnes. Technol. (2018) 349–353.
[8] X.X. Dong, E.A. Nyberg, S. Ji, A die-cast magnesium alloy for applications at elevated temperatures, Magnes. Technol. (2020) 31–36.
[9] M. Pekguleryuz, M. Celikin, Creep resistance in magnesium alloys, Int. Mater. Rev. 55 (2010) 197–217.
[10] M. Easton, M.A. Gibson, S.M. Zhu, T. Abbott, J.F. Nie, C.J. Bettles, G. Savage, Development of magnesium-rare earth die-casting alloys, Magnes. Technol. (2018) 329–336.
[11] J.P. Weiler, J.T. Wood, Modeling the tensile failure of cast magnesium alloys, J. Alloys Compd. 537 (2012) 133–140.
[12] A.A. Luo, Recent magnesium alloy development for elevated temperature applications, Int. Mater. Rev. 49 (2004) 13–30.
[13] P. Humble, Towards a cheap creep resistant magnesium alloy, Mater. Forum 21 (1997) 45–56.
[14] S.M. Zhu, M.A. Easton, T.B. Abbott, J.F. Nie, M.S. Dargusch, N. Hort, M.A. Gibson, Evaluation of magnesium die-casting alloys for elevated temperature applications: microstructure, tensile properties, and creep resistance, Metall. Mater. Trans. A 46A (2015) 3543–3554.
[15] J.E. Hillis, S.O. Shook, Composition and performance of an improved magnesium AS41 alloy, SAE Tech. Pap. (1989) 890205.
[16] M.O. Pekguleryuz, E. Baril, Development of creep resistant Mg-Al-Sr alloys, Magnes. Technol. (2001) 119–125.
[17] F. Buch, S. Schumann, H. Friedrich, E. Aghion, B. Bronfin, B.L. Mordike, M. Bamberger, D. Eliezer, New die-casting alloy Mri153 for power-train applications, Magnes. Technol. (2002) 61–68.
[18] B.R. Powell, V. Rezhets, M.P. Balogh, R.A. Waldo, The relationship between microstructure and creep behavior in AE42 magnesium die castings, Magnes. Technol. (2001) 175–182.
[19] E. Aghion, N. Moscovitch, A. Arnon, Solidification characteristics of newly developed die cast magnesium alloy MRI153M, Mater. Sci. Technol. 23 (2007) 270–275.
[20] E. Aghion, B. Bronfin, F. Von Buch, S. Schumann, H. Friedrich, Newly developed magnesium alloys for powertrain applications, JOM 55 (2003) 30–33.
[21] E. Aghion, N. Moscovitch, A. Arnon, Mechanical properties of die-cast magnesium alloy MRI 230D, J. Mater. Eng. Perform. 18 (2009) 912–916.
[22] B.R. Powell, V. Rezhets, A.A. Luo, J.J. Bommarito, B.L. Tiwari, Creep resistant magnesium alloy die casting, US Patent (2001) 6264763.
[23] S.M. Zhu, J.F. Nie, M.A. Gibson, M.A. Easton, P. Bakke, Microstructure and creep behavior of high-pressure die-cast magnesium alloy AE44, Metall. Mater. Trans. A 43A (2012) 4137–4144.
[24]] I.P. Moreno, T.K. Nandy, J.W. Jones, J.E. Allison, T.M. Pollock, Microstructural stability and creep of rare-earth containing magnesium alloys, Scr. Mater. 48 (2003) 1029–1034.
[25] X.X. Dong, L.Y. Feng, S.H. Wang, E.A. Nyberg, S. Ji, A new die-cast magnesium alloy for applications at higher elevated temperatures of 200–300 °C, J. Magnes. Alloy. 9 (2021) 90–101.
[26]] I.P. Moreno, T.K. Nandy, J.W. Jones, J.E. Allison, T.M. Pollock, Microstructural characterization of a die-cast magnesium-rare earth alloy, Scr. Mater. 45 (2001) 1423–1429.
[27]] S.M. Zhu, M.A. Gibson, M.A. Easton, J.F. Nie, The relationship between microstructure and creep resistance in die-cast magnesium–rare earth alloys, Scr. Mater. 63 (2010) 698–703.
[28] D. Choudhuri, D. Jaeger, M.A. Gibson, R. Banerjee, Role of Zn in enhancing the creep resistance of Mg–RE alloys, Scr. Mater. 86 (2014) 32–35.
[29] S. Gavras, S.M. Zhu, J.F. Nie, M.A. Gibson, M.A. Easton, On the microstructural factors affecting creep resistance of die-cast Mg–La-rare earth (Nd, Y or Gd) alloys, Mater. Sci. Eng. A 675 (2016) 65–75.
[30] S. Abaspour, C.H. Cáceres, Thermodynamics-based selection and design of creepresistant cast Mg alloys, Metall. Mater. Trans. A 46 (2015) 5972–5988.
[31] J.F. Nie, N.C. Wilson, Y.M. Zhu, Z. Xu, Solute clusters and GP zones in binary Mg–RE alloys, Acta Mater. 106 (2016) 260–271.
[32] Y. Matsuoka, K. Matsuda, K. Watanabe, J. Nakamura, W. Lefebvre, D. Nakagawa, S.Ikeno S.Saikawa, Precipitation sequence in the Mg–Gd–Y system investigated by HRTEM and HAADF-STEM, Mater. Trans. 55 (2014) 1051–1057.
[33] R.A. Karnesky, M.E. van Dalen, D.C. Dunand, D.N. Seidman, Effects of substituting rare-earth elements for scandium in a precipitation-strengthened Al–0.08 at.%*Sc* alloy, Scr. Mater. 55 (2006) 437–440.
[34] R.A. Karnesky, D.N. Seidman, D.C. Dunand, Creep of Al-*Sc* microalloys with rare-earth element additions, Mater. Sci. Forum 519–521 (2006) 1035–1040.
[35] M.E. Krug, A. Werber, D.C. Dunand, D.N. Seidman, Core–shell nanoscale precipitates in Al–0.06 at.% *Sc* microalloyed with Tb, Ho, Tm or Lu, Acta Mater. 58 (2010) 134–145.
[36] D. Amberger, P. Eisenlohr, M. Göken, On the importance of a connected hard-phase skeleton for the creep resistance of Mg alloys, Acta Mater. 60 (2012) 2277–2289.
[37] N. Mo, I. McCarroll, Q.Y. Tan, A. Ceguerra, Y. Liu, J. Cairney, H. Dieringa, Y.D. Huang, B. Jiang, F.S. Pan, M. Bermingham, M.X. Zhang, Understanding solid solution strengthening at elevated temperatures in a creep-resistant Mg–Gd–Ca alloy, Acta Mater. 181 (2019) 185–199.
[38] J.F. Nie, K. Oh-ishi, X. Gao, K. Hono, Solute segregation and precipitation in a creep-resistant Mg–Gd–Zn alloy, Acta Mater. 56 (2008) 6061–6076.
[39] S.M. Zhu, T.B. Abbott, M.A. Gibson, J.F. Nie, M.A. Easton, The influence of minor Mn additions on creep resistance of die-cast Mg–Al–RE alloys, Mater. Sci. Eng. A 682 (2017) 535–541.
[40] Q. Yang, K. Guan, B.S. Li, S.H. Lv, F.Z. Meng, W. Sun, Y.Q. Zhang, X.J. Liu, J. Meng, Microstructural characterizations on Mn-containing intermetallic phases in a high-pressure die-casting Mg–4Al–4RE–0.3Mn alloy, Mater. Charact. 132 (2017) 381–387.
[41] M. Almgren, H. Assarsson, S. Hjalmarsson, X.X. Dong, S. Ji, E.A. Nyberg, P. Orestig, WIPO Patent (2020) WO2020171758A1.
[42] K. Momma, F. Izumi, *VESTA 3* for three-dimensional visualization of crystal, volumetric and morphology data, J. Appl. Crystallogr. 44 (2011) 1272–1276.
[43] V. Sklenicka, K. Kucharova, M. Svoboda, M. Kvapilova, J. Dvorak, P. Kra, Creep behaviour of unreinforced and reinforced QE22 magnesium alloy: a comparison, Kov. Mater. 58 (2020) 71–82.
[44] A. Kielbus, T. Rzychon, Mechanical and creep properties of Mg-4Y-3RE and Mg3Nd-1Gd magnesium alloy, Procedia Eng. 10 (2011) 1835–1840.
[45] C.J. Bettles, M.A. Gibson, S.M. Zhu, Microstructure and mechanical behaviour of an elevated temperature Mg-rare earth based alloy, Mater. Sci. Eng. A 505 (2009) 6–12.
[46] B.L. Mordike, Creep-resistant magnesium alloys, Mater. Sci. Eng. A 324 (2002) 103–112.
[47] B. Smola, I. Stulıková, J. Pelcova, B.L. Mordike, Significance of stable and metastable phases in high temperature creep resistant magnesium–rare earth base alloys, J. Alloy. Compd. 378 (2004) 196–201.
[48] V. Janik, D.D. Yin, Q.D. Wang, S.M. He, C.J. Chen, Z. Chen, C.J. Boehlert, The elevated temperature mechanical behavior of peak-aged Mg–10Gd–3Y–0.4 Zr alloy, Mater. Sci. Eng. A 528 (2011) 3105–3112.
[49] I.A. Anyanwu, S. Kamado, Y. Kojima, Creep properties of Mg-Gd-Y-Zr alloys, Mater. Trans. 42 (2001) 1212–1218.
[50] I. Stulíková, B. Smola, B.L. Mordike, New high temperature creep resistant Mg–YNd–*Sc*–Mn alloy, Phys. Status Solidi A 190 (2002) 5–7.
[51] M.B. Yang, J. Xiao, L.X. Zhong, H. Lin, W.W. Shen, J. Liu, F.S. Pan, CN Patent (2018) 107739947A.
[52] Q. Wang, H. Tomeoku, J. Gu, G. Yan, CN Patent (2009) 100545286C.
[53] W.F. Xu, Y. Zhang, L.M. Peng, W.J. Ding, J.F. Nie, Formation of denuded zones in crept Mg–2.5Gd–0.1Zr alloy, Acta Mater. 84 (2015) 317–329.
[54] V.I. Evdokimenko, P.I. Kripyakevich, The crystal structures of magnesium-rich compounds in the systems La-Mg, Ce- Mg, and Nd-Mg, Sov. Phys. Crystallogr. 8 (1963) 186–193.
[55] X.R. Hua, Q. Yang, D.D. Zhang, F.Z. Meng, C. Chen, Z.H. You, J.H. Zhang, S.H. Lv, J. Meng, Microstructures and mechanical properties of a newly developed high-pressure die casting Mg-Zn-RE alloy, J. Mater. Sci. Technol. 53 (2020) 174–184.
[56] N.C. Baenziger, J.J. Hegenbarth, Gadolinium and dysprosium intermetallic phases. III. The structures of Gd_3Al_2, Dy_3Al_2, Gd_5Ge_3, Dy_5Ge_3 and $DyAl_3$, Acta Crystallogr. 17 (1964) 620–621.
[57] J. Li, J.L. Wu, L. Jin, M. Celikin, F.H. Wang, S. Dong, J. Dong, The role of dislocation-solute interactions on the creep behaviour of binary Mg–RE alloys, Sci. Rep. 11 (2021) 2860.

[58] Y. Ma, A. Addad, G. Ji, M.X. Zhang, W. Lefebvre, Z. Chen, V. Ji, Atomic-scale investigation of the interface precipitation in a TiB_2 nanoparticles reinforced Al–Zn–Mg–Cu matrix composite, Acta Mater. 185 (2020) 287–299.
[59] A. Śalebarski, Anomalous change of the curie temperature of $GdAl_2$, Phys. Status Solidi A 46 (1978) 29–34.
[60] M. Razazi, R.N. Amini, B.B. Eshov, A.B. Badalov, Preparation of physical and chemical and thermodynamic properties of aluminum alloys-cerium, Mater. Sci. Res. India 9 (2012) 1–7.
[61] D.K. Saini, R. Gope, A. Mandal, Effect of alloying elements on thermal stability of Aluminium-Cerium based alloys, Res. Sq. (2020) 1–12, doi:10.21203/rs.3.rs-67587/v1.
[62] S.K. Woo, C.D. Yim, Y.M. Kim, B.S. You, Effect of Ca and Y on corrosion behavior of extruded AZ series Mg alloys, Magnes. Technol. (2015) 323–326.
[63] G. Pettersen, H. Westengen, R. Hoier, O. Lohne, Microstructure of a pressure die cast magnesium-4 wt.% aluminium alloy modified with rare earth additions, Mater. Sci. Eng. A 207 (1996) 115–120.
[64] S.M. Zhu, T.B. Abbott, M.A. Gibson, J.F. Nie, M.A. Easton, Age hardening in die-cast Mg–Al–RE alloys due to minor Mn additions, Mater. Sci. Eng. A 656 (2016) 34–38.
[65] Q. Yang, S.H. Lv, F.Z. Meng, K. Guan, B.S. Li, X.H. Zhang, J.Q. Zhang, X.J. Liu, J. Meng, Detailed structures and formation mechanisms of well-known $Al_{10}RE_2Mn_7$ phase in die-cast Mg–4Al–4RE–0.3Mn alloy, Acta Metall. Sin. Engl. 32 (2019) 178–186.